CMOS compatible metamaterial absorbers for hyperspectral medium wave infrared imaging and sensing applications

JAMES GRANT,* MITCHELL KENNEY, YASH D. SHAH, IVONNE ESCORCIA-CARRANZA, AND DAVID R. S. CUMMING

Microsystems Technology Group, School of Engineering, University of Glasgow, G12 8LT, United Kingdom
james.grant@glasgow.ac.uk

Abstract: We experimentally demonstrate a CMOS compatible medium wave infrared metal-insulator-metal (MIM) metamaterial absorber structure where for a single dielectric spacer thickness at least 93% absorption is attained for 10 separate bands centred at 3.08, 3.30, 3.53, 3.78, 4.14, 4.40, 4.72, 4.94, 5.33, 5.60 μm. Previous hyperspectral MIM metamaterial absorber designs required that the thickness of the dielectric spacer layer be adjusted in order to attain selective unity absorption across the band of interest thereby increasing complexity and cost. We show that the absorption characteristics of the hyperspectral metamaterial structures are polarization insensitive and invariant for oblique incident angles up to 25° making them suitable for practical implementation in an imaging system. Finally, we also reveal that under TM illumination and at certain oblique incident angles there is an extremely narrowband Fano resonance (Q > 50) between the MIM absorber mode and the surface plasmon polariton mode that could have applications in hazardous/toxic gas identification and biosensing.

References and links

1. R. Usamentiaga, P. Venegas, J. Guerediaga, L. Vega, J. Molleda, and F. G. Bulnes, "Infrared thermography for temperature measurement and non-destructive testing," Sensors (Basel) **14**(7), 12305–12348 (2014).
2. C.-C. Chen Attenuation of Electromagnetic Radiation by Haze, Fog, Clouds, and Rain," (1975).
3. C. Xie, M. Aziz, V. Pusino, A. Khalid, M. Steer, I. G. Thayne, M. Sorel, and D. R. S. Cumming, "Single-chip, mid-infrared array for room temperature video rate imaging," Optica **4**(12), 1498 (2017).
4. D. Gibson and C. MacGregor, "A novel solid state non-dispersive infrared CO2 gas sensor compatible with wireless and portable deployment," Sensors **13**(6), 7079–7103 (2013).
5. A. Krier, *Mid-Infrared Semiconductor Optoelectronics* (Springer London, 2006).
6. *VISIMID GigE PoE Broadband Camera Specifications* (2018).
7. D. Pacifici, H. J. Lezec, L. A. Sweatlock, R. J. Walters, and H. A. Atwater, "Universal optical transmission features in periodic and quasiperiodic hole arrays," Opt. Express **16**(12), 9222–9238 (2008).
8. A. Kristensen, J. K. W. Yang, S. I. Bozhevolnyi, S. Link, P. Nordlander, N. J. Halas, and N. A. Mortensen, "Plasmonic colour generation," Nat. Rev. Mater. **2**(1), 16088 (2016).
9. I. J. H. McCrindle, J. Grant, T. D. Drysdale, and D. R. S. Cumming, "Hybridization of optical plasmonics with terahertz metamaterials to create multi-spectral filters," Opt. Express **21**(16), 19142–19152 (2013).
10. Y. D. Shah, J. Grant, D. Hao, M. Kenney, V. Pusino, and D. R. S. Cumming, "A symmetry-breaking selective plasmonic metasurface Ultra-narrow linewidth polarization-insensitive filter using a symmetry-breaking selective plasmonic metasurface," ACS Photonics **5**(2), 663 (2017).
11. H. T. Chen, A. J. Taylor, and N. Yu, "A review of metasurfaces: Physics and applications," Rep. Prog. Phys. **79**(7), 076401 (2016).
12. A. Arbabi, Y. Horie, M. Bagheri, and A. Faraon, "Dielectric metasurfaces for complete control of phase and polarization with subwavelength spatial resolution and high transmission," Nat. Nanotechnol. **10**(11), 937–943 (2015).
13. N. I. Landy, S. Sajuyigbe, J. J. Mock, D. R. Smith, and W. J. Padilla, "Perfect metamaterial absorber," Phys. Rev. Lett. **100**(20), 207402 (2008).

14. X. Liu, T. Tyler, T. Starr, A. F. Starr, N. M. Jokerst, and W. J. Padilla, "Taming the Blackbody with Infrared Metamaterials as Selective Thermal Emitters," Phys. Rev. Lett. **107**(4), 045901 (2011).
15. H. T. Chen, "Interference theory of metamaterial perfect absorbers," Opt. Express **20**(7), 7165–7172 (2012).
16. J. Grant, Y. Ma, S. Saha, L. B. Lok, A. Khalid, and D. R. S. Cumming, "Polarization insensitive terahertz metamaterial absorber," Opt. Lett. **36**(8), 1524–1526 (2011).
17. J. Grant, I. J. McCrindle, C. Li, and D. R. Cumming, "Multispectral metamaterial absorber," Opt. Lett. **39**(5), 1227–1230 (2014).
18. C. M. Watts, X. Liu, and W. J. Padilla, "Metamaterial Electromagnetic Wave Absorbers," Adv. Mater. **24**(23), OP98–OP120 (2012).
19. Y. Q. Ye, Y. Jin, and S. L. He, "Omnidirectional, polarization-insensitive and broadband thin absorber in the terahertz regime," J. Opt. Soc. Am. B **27**(3), 498–504 (2010).
20. J.-Y. Jung, J. Lee, D.-G. Choi, J.-H. Choi, J.-H. Jeong, E.-S. Lee, and D. P. Neikirk, "Wavelength-Selective Infrared Metasurface Absorber for Multispectral Thermal Detection," IEEE Photonics J. **7**(6), 1–10 (2015).
21. S. Song, Q. Chen, L. Jin, and F. Sun, "Great light absorption enhancement in a graphene photodetector integrated with a metamaterial perfect absorber," Nanoscale **5**(20), 9615–9619 (2013).
22. Q. Chen, F. Sun, and S. Song, "Subcell misalignment in vertically cascaded metamaterial absorbers," Opt. Express **21**(13), 15896–15903 (2013).
23. X. Hu, G. Xu, L. Wen, H. Wang, Y. Zhao, Y. Zhang, D. R. S. Cumming, and Q. Chen, "Metamaterial absorber integrated microfluidic terahertz sensors," Laser Photonics Rev. **10**(6), 962–969 (2016).
24. T. D. Dao, K. Chen, S. Ishii, A. Ohi, T. Nabatame, M. Kitajima, and T. Nagao, "Infrared Perfect Absorbers Fabricated by Colloidal Mask Etching of Al–Al $_2$ O $_3$ –Al Trilayers," ACS Photonics **2**(7), 964–970 (2015).
25. G. Dayal and S. Anantha Ramakrishna, "Design of multi-band metamaterial perfect absorbers with stacked metal-dielectric disks," J. Opt. **15**(5), 1–7 (2013).
26. T. Maier and H. Brückl, "Wavelength-tunable microbolometers with metamaterial absorbers," Opt. Lett. **34**(19), 3012–3014 (2009).
27. T. Maier and H. Brueckl, "Multispectral microbolometers for the midinfrared," Opt. Lett. **35**(22), 3766–3768 (2010).
28. J. Y. Suen, K. Fan, J. Montoya, C. Bingham, V. Stenger, S. Sriram, and W. J. Padilla, "Multifunctional metamaterial pyroelectric infrared detectors," Optica **4**(2), 276 (2017).
29. J. Grant, I. Escorcia-Carranza, C. Li, I. J. H. McCrindle, J. Gough, and D. R. S. Cumming, "A monolithic resonant terahertz sensor element comprising a metamaterial absorber and micro-bolometer," Laser Photonics Rev. **7**(6), 1043–1048 (2013).
30. D. Shrekenhamer, W. Xu, S. Venkatesh, D. Schurig, S. Sonkusale, and W. J. Padilla, "Experimental Realization of a Metamaterial Detector Focal Plane Array," Phys. Rev. Lett. **109**(17), 177401 (2012).
31. F. B. P. Niesler, J. K. Gansel, S. Fischbach, and M. Wegener, "Metamaterial metal-based bolometers," Appl. Phys. Lett. **100**(20), 2012–2015 (2012).
32. S. Kang, Z. Qian, V. Rajaram, A. Alu, and M. Rinaldi, "Ultra narrowband infrared absorbers for omni-directional and polarization insensitive multi-spectral sensing microsystems," in *TRANSDUCERS 2017 - 19th Int. Conf. Solid-State Sensors, Actuators Microsystems* (2017), pp. 886–889.
33. E. D. Palik, *Handbook of Optical Constants of Solids* (Elsevier Science & Tech, 1985).
34. S. Yokogawa, S. P. Burgos, and H. A. Atwater, "Plasmonic color filters for CMOS image sensor applications," Nano Lett. **12**(8), 4349–4354 (2012).
35. W. R. Zhu, X. P. Zhao, B. Y. Gong, L. H. Liu, and B. Su, "Optical metamaterial absorber based on leaf-shaped cells," Appl. Phys. A **102**(1), 147–151 (2011).
36. S. A. Maier, *Plasmonics : Fundamentals and Applications* (Springer, 2007).
37. U. Fano, "Effects of Configuration Interaction on Intensities and Phase Shifts," Phys. Rev. **124**(6), 1866–1878 (1961).
38. J. Kischkat, S. Peters, B. Gruska, M. Semtsiv, M. Chashnikova, M. Klinkmüller, O. Fedosenko, S. Machulik, A. Aleksandrova, G. Monastyrskyi, Y. Flores, and W. T. Masselink, "Mid-infrared optical properties of thin films of aluminum oxide, titanium dioxide, silicon dioxide, aluminum nitride, and silicon nitride," Appl. Opt. **51**(28), 6789–6798 (2012).
39. I. J. H. Mccrindle, J. Grant, T. D. Drysdale, and D. R. S. Cumming, "Multi-spectral materials: Hybridisation of optical plasmonic filters and a terahertz metamaterial absorber," Adv. Opt. Mater. **2**(2), 149–153 (2014).
40. I. J. H. McCrindle, J. P. Grant, L. C. P. Gouveia, and D. R. S. Cumming, "Infrared plasmonic filters integrated with an optical and terahertz multi-spectral material," Phys. Status Solidi Appl. Mater. Sci. **212**(8), 1625–1633 (2015).
41. J. Grant, I. J. H. McCrindle, and D. R. S. Cumming, "Multi-spectral materials: hybridisation of optical plasmonic filters, a mid infrared metamaterial absorber and a terahertz metamaterial absorber," Opt. Express **24**(4), 3451–3463 (2016).

1. Introduction

Medium wave infrared (MWIR) radiation, defined as the region between 3 and 5 μm of the electromagnetic spectrum, has several important characteristics. At room temperature all materials emit MWIR. This thermal signature can be captured by a suitable detector and the

object readily identified [1]. Moreover, unlike visible radiation, MWIR is transparent to cloud and fog [2]. Small biomolecules such as carbohydrates and pharmaceuticals with ~10-30 atoms have intramolecular vibrations in the MWIR range while a number of odourless and toxic/flammable gases such as carbon monoxide (CO), nitric oxide (NO) and methane (CH_4) have absorption bands in the MWIR region [3]. These properties have led to a number of applications in sectors such as medical diagnostics, detection and classification of biological materials, environmental monitoring and hazardous gas detection [4,5].

However, widespread adoption of these applications has been hindered by the high cost of the components, primarily the detectors. Photodiode technology based on mercury cadmium telluride (MCT) or indium antimonide (InSb) material systems have traditionally dominated the MWIR imaging market however more recently the bolometric approach has become more attractive due to the ability to operate at room temperature and recent advances in micro-electro-mechanical systems manufacturing techniques resulting in reduced cost. Nowadays bolometric based 640 x 512 focal plane array imagers with pixel sizes of 17 μm and video rate read-out speeds are commercially available at significantly lower cost than their MCT or InSb photodiode equivalents [6].

For hyperspectral applications, such as hazardous gas detection or environmental monitoring, components must be added to the imaging set-up in the form of multi-layer filters or interferometers, increasing system complexity, cost and acquisition time. The ideal hyperspectral imager should have no moving parts and therefore be compact, have high spectral resolving power, high spatial resolution and high sensitivity. However, at present no current technology fulfils these needs since filter wheel systems have low operational speed while interferometers require a high precision mechanical scanner coupled with a wide bandwidth detector.

Metamaterials, and their 2D counterpart metasurfaces, have recently emerged as alternatives to traditional dispersive or multi-layer interference filters [7–10]. Meta-structures are constructed from sub-wavelength thick films of metal and/or dielectric and offer the advantage that the transmission/reflection/absorption characteristics can be engineered simply by changing the geometry of the constituent meta-atoms [11,12]. This geometry engineering is typically done using high-precision lithography techniques employed in the microelectronics industry and is therefore inherently low-cost. Metamaterial absorbers in particular have attracted significant attention due to the lack of natural materials that selectively absorb in the infrared (IR) and terahertz (THz) range [13–17]. A metamaterial absorber is typically constructed of a metal-insulator-metal (MIM) stack where the top layer of metal is comprised of a so called electric ring resonator (ERR) separated by a dielectric layer from a bottom layer that is a continuous metal ground-plane. The ERR couples strongly to the incident electric field while the addition of the dielectric and ground plane enables coupling of the magnetic component of the incident light to the structure. Modifying the ERR geometry and the dielectric thickness allows independent tuning of the electric and magnetic response respectively, so that unity absorption is attained when the free space impedance (Z_0 = μ_0/ε_0 = 377 Ω) matches that of the device impedance ($Z = \mu/\varepsilon$) [18]. The fundamental resonant frequency of a MIM metamaterial absorber is [19]:

$$f_m = \frac{1}{\sqrt{LC/2}}$$

where f_m is the resonant frequency position, L in the inductance and C is the capacitance. The capacitance is determined by the area of the ERR and the insulating layer composition and thickness while the inductance is determined by the length and width of the ERR. In practice the ERR geometry and real part of the refractive index of the spacer material predominantly determines the resonant frequency peak position while the thickness and loss tangent of the spacer material between the two conducting layers determines the absorption magnitude [19]. Single band, broadband and hyperspectral MIM metamaterial absorber structures have been

demonstrated across the entire electromagnetic spectrum, from the mm wave to the visible, and have applications in imaging, energy harvesting and biosensing [20–25]. In addition, metamaterial absorbers, being extremely thin periodic structures, lend themselves to integration with detectors such as bolometers and pyrometers to form imaging arrays [26–31]. Furthermore, monolithic integration of the spectral selection component, i.e. the metamaterial absorber, directly in the pixel offers the advantage of miniaturization and obviates the need for external wavelength selection components, further reducing manufacturing cost and system complexity.

A major challenge, until now unsolved, is to establish a geometry whereby selective high absorption, i.e. >90%, is attained for a single dielectric thickness throughout the waveband of interest e.g. MWIR or LWIR using CMOS compatible materials. Previous work on MWIR MIM metamaterial absorbers with square shaped ERRs and a 120 nm Si_3N_4 spacer layer found that the absorption magnitude dropped to as low 64% across the 3-5 μm waveband [27]. The authors stated that to attain higher absorption magnitudes the spacer layer thickness must be optimised for each wavelength. To attain high absorption at longer wavelengths the spacer layer thickness must also increase. For practical applications it would be inefficient and costly to fabricate a bolometric based hyperspectral MWIR imager that necessitates several lithographic procedures to define different dielectric spacer thicknesses to attain high absorption for each hyperspectral band. Kang et al. demonstrated hyperspectral MIM metamaterial absorbers spanning the MWIR range using a single dielectric thickness however the absorption efficiency was as low as 80% and Au metal employed, which is not CMOS compatible [32].

Here we experimentally demonstrate a CMOS compatible metamaterial absorber structure where for a single dielectric spacer thickness at least 93% absorption is attained for 10 separate bands centred at 3.08, 3.30, 3.53, 3.78, 4.14, 4.40, 4.72, 4.94, 5.33, 5.60 μm. We study experimentally and via simulations the absorption characteristics for both normally incident radiation and obliquely incident radiation of 40 MWIR metamaterial absorbers where the ERR arm length and dielectric thickness are varied. We also show that the absorption characteristics of all the hyperspectral metamaterial structures are invariant up to incident angles up to 25°.
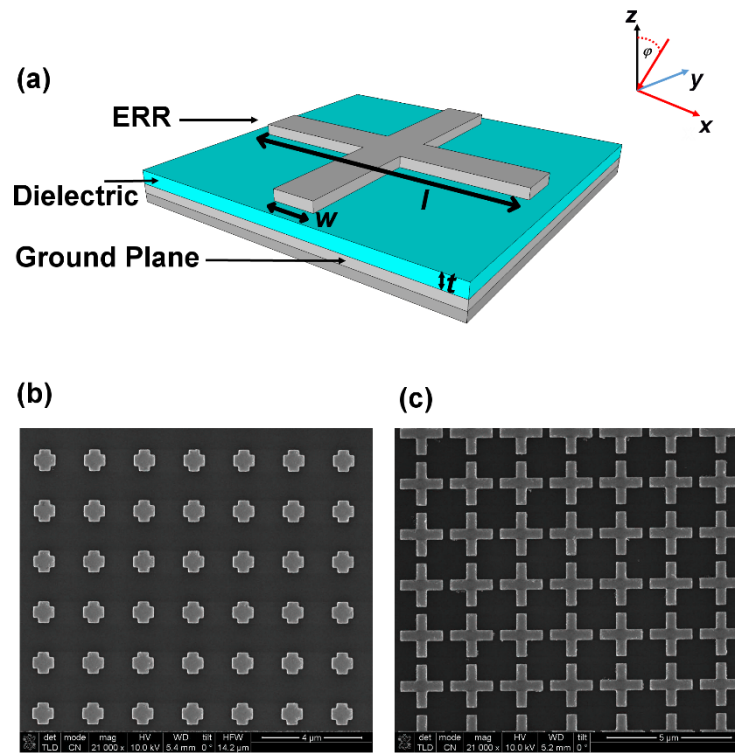
Fig. 1. Concept and SEM images of fabricated CMOS compatible MWIR metamaterial absorbers. (a) 3D schematic of the metamaterial absorber. A Ti/Al ground plane is separated from a Ti/Al ERR by a SiO$_2$ dielectric layer of thickness, t. The ERR has a variable cross arm length, l, from 800 to 1700 nm and a fixed arm width, w, of 400 nm. (b) Scanning electron microscope (SEM) image of a MWIR metamaterial absorber with l = 800 nm. (c) SEM image of a MWIR metamaterial absorber with l = 1700 nm. The unit cell period is 2000 nm.

2. Simulation, Fabrication and Experimental Characterisation

A 3D schematic diagram depicting the unit cell of a typical CMOS compatible MWIR metamaterial absorber is shown in Fig. 1(a). A Ti/Al (10/90 nm thick) cross-shaped ERR is separated from a Ti/Al (10/90 nm thick) metallic ground plane by a silicon dioxide (SiO$_2$) layer of thickness, t. The ERR cross arm width, w, is fixed at 400 nm while the arm length, l, is varied from 800 to 1700 nm in steps of 100 nm and the SiO$_2$ thickness varied from 25 to 100 nm in steps of 25 nm. The unit cell period is 2000 nm. In all, 40 different MWIR designs were fabricated and experimentally characterised and the results compared to simulations. Lumerical FDTD simulation software was used to determine the spectral response, incident angle dependence and absorption distribution of the MWIR MM absorbers. For the spectral response simulations a plane wave was normally incident (z direction) on the Al ERR/SiO$_2$/Al ground plane stack. Values obtained from Palik were used for both the Al and SiO$_2$ [33]. For all normal incidence simulations the electric field was orientated in the x plane (i.e. TM polarisation). A mesh grid with an x and y cell size of 50 nm and a z cell size of 5 nm was defined around the structure. Taking advantage of the inherent symmetry of the MM absorber structure and to reduce computation demands, symmetric and anti-symmetric boundary conditions were used in the x and y and perfectly matched layers (PML) were used in the z boundaries. A reflection monitor was located behind the source to record the reflected radiation from the structure. On account of the ground plane the transmission through the metamaterial structure is zero therefore the absorption is expressed as $1 - R$, where R is the

reflection magnitude. For the incident angle dependence simulations a similar set-up was employed with the exception that Bloch boundaries were used in the x and y. For each metamaterial design 60 simulations were performed for incident polar (*xz*) angles ranging from 0° to 60°.
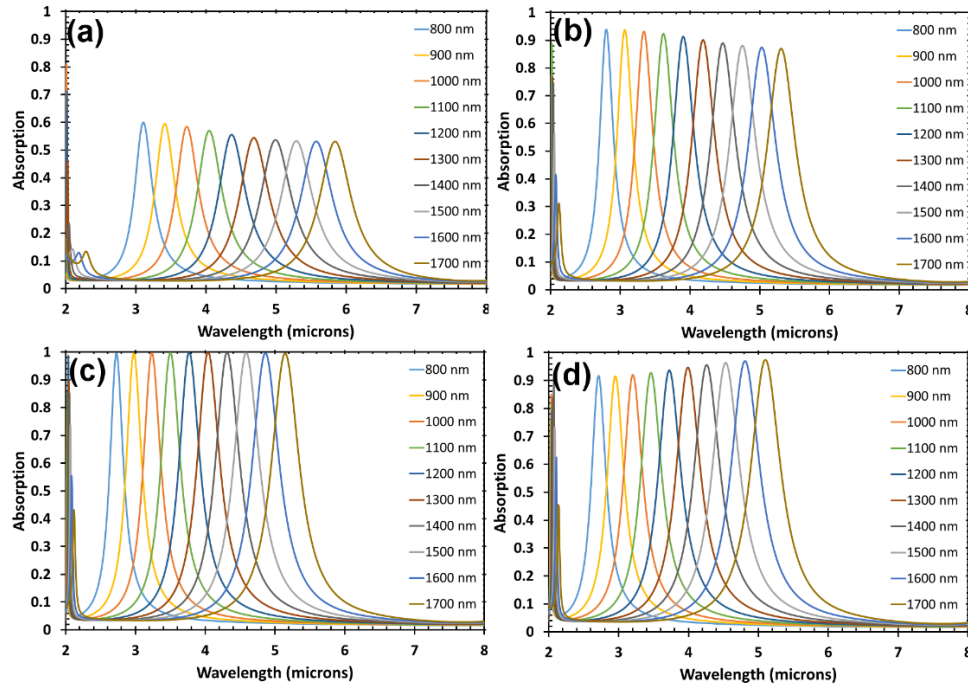

Fig. 2. Simulation data for the CMOS compatible MWIR metamaterial absorbers. Simulated absorption spectra for metamaterial absorbers with fixed arms widths, w = 400 nm, and arm lengths, l, varying from 800 to 1700 nm for SiO$_2$ dielectric thickness of (a) 25 nm, (b) 50 nm, (c) 75 nm and (d) 100 nm.

The simulated absorption spectra plots for ERR arm lengths from 800 to 1700 nm are shown in Fig. 2 for SiO$_2$ thicknesses of (a) 25 nm, (b) 50 nm, (c) 75 nm and (d) 100 nm. Comparing the simulation curves there are several noticeable features. Firstly, for all thicknesses we observe, as anticipated, that the peak absorption wavelength position increases with increasing cross arm length. Secondly, for all 10 ERR designs, the absorption magnitude increases as the SiO$_2$ thickness increases from 25 nm to 75 nm. The average peak absorption magnitude is 55.4% and 90.2% for SiO$_2$ thicknesses of 25 nm and 50 nm respectively. What is more remarkable is that for a 75 nm thick SiO$_2$ layer the minimum absorption magnitude is 99% for the 10 different ERR designs traversing the entire MWIR region (2.72 μm to 5.17 μm). As the SiO$_2$ thickness increases further to 100 nm there is a slight decrease in the absorption magnitude to an average of 94%. Taking a closer look at Figs. 2(b) and 2(d) we see that there are two distinctly opposite trends in terms of absorption magnitude and increasing cross arm length. For the 50 nm thick SiO$_2$ metamaterial absorbers [Fig. 2(b)] the absorption magnitude steadily decreases with increasing cross arm length while for the 100 nm thick SiO$_2$ metamaterial absorbers [Fig. 2(d)] the absorption magnitude steadily increases with cross arm length.

To fabricate the MWIR MM absorbers first the Ti/Al (10/90 nm) ground plane was evaporated via electron beam deposition onto a 550 μm thick Si substrate. Next, the requisite thickness of SiO$_2$ (25/50/75/100 nm) was deposited via a plasma enhanced chemical vapor deposition (PECVD) process. Finally, electron beam lithography was used to pattern a bi-

layer of poly(methyl methacrylate) (PMMA) resist to form the cross shaped ERR structures of fixed width (0.4 μm) and varying lengths (0.8 μm to 1.7 μm). After development in 1:1 isopropyl alcohol: methyl isobutyl ketone (IPA: MIBK) for 30 seconds at 23°C a 10/90 nm Ti/Al layer was evaporated and lift-off performed by immersing the sample in a beaker of acetone at 50°C. Each MM design spanned an area of 12 x 12 mm. Scanning electron microscope (SEM) images of fabricated MM absorbers with a cross arm length of 800 nm and a cross arm length of 1700 nm are shown in Figs. 2(b) and 2(c) respectively.

Characterisation of the MWIR MM absorbers was performed using a Bruker IFS 66v/S Fourier transform infrared spectrometer (FTIR) in reflection mode at 30° incidence. The reflection and transmission measurements were performed using a SiC globar source, KBr beamsplitter and a deuterated L-alanine-doped triglycine sulfate (DLATGS) pyroelectric detector. The reflection spectra was normalised to a gold mirror through a 10 mm aperture.
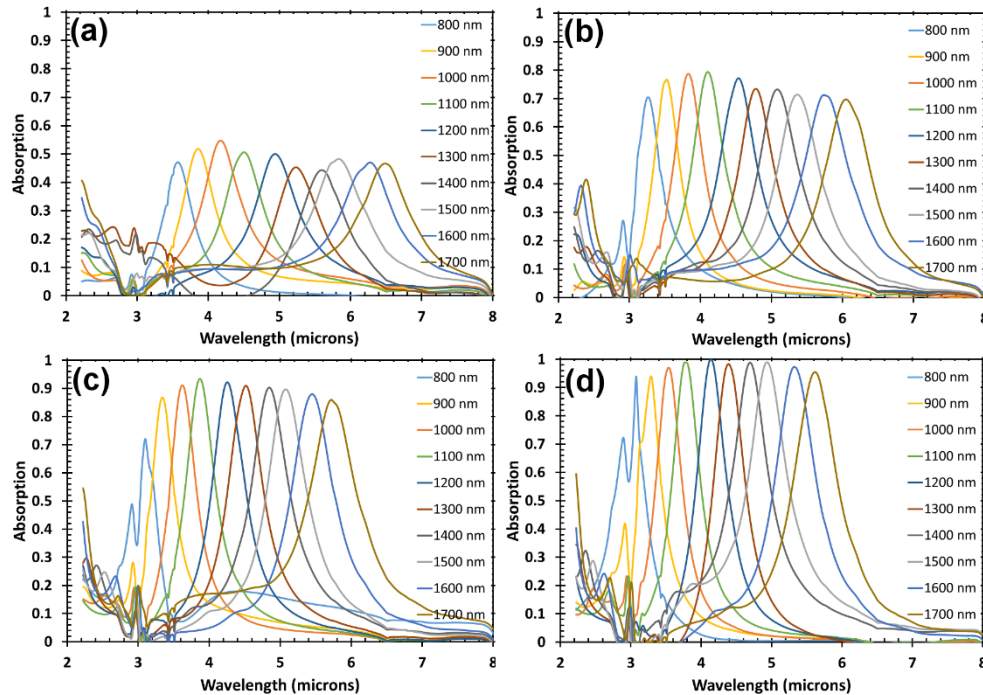

Fig. 3. Experimental data for the CMOS compatible MWIR metamaterial absorbers. Experimental absorption spectra for metamaterial absorbers with fixed arms widths, $w = 400$ nm, and arm lengths, l, varying from 800 to 1700 nm for SiO_2 dielectric thickness of (a) 25 nm, (b) 50 nm, (c) 75 nm and (d) 100 nm.

The experimental absorption spectra plots for ERR arms lengths from 800 to 1700 nm are shown in Fig. 3 for SiO_2 thicknesses of (a) 25 nm, (b) 50 nm, (c) 75 nm and (d) 100 nm. The experimental spectral responses show similar trends to those simulated; the peak absorption wavelength position red shifts with increasing cross-arm length and the absorption magnitude is strongly dependent on the SiO_2 thickness. However, in contrast to the simulated data the optimum SiO_2 thickness to attain the maximum absorption is 100 nm, not 75 nm. For a 100 nm thick SiO_2 layer the peak absorption magnitude of the 10 MWIR absorbers is at least 93% and the average peak magnitude is 97%. The peak absorption wavelength positions for the 100 nm thick SiO_2 metamaterial absorbers are 3.08, 3.30, 3.53, 3.78, 4.14, 4.40, 4.72, 4.94, 5.33, 5.60 μm. This is, to the best of our knowledge, the first experimental demonstration of a spectrally selective metamaterial absorber that has greater than 90% absorption magnitude across the entire MWIR region for a single dielectric spacer layer thickness.
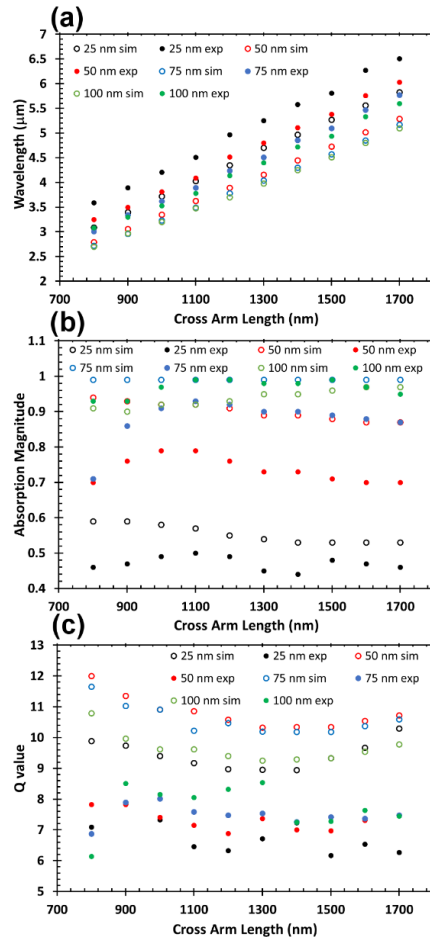
Fig. 4. Analysis and comparison of simulation and experimental data for the CMOS compatible MWIR metamaterial absorbers. Simulated and experimental comparison of (a) peak absorption wavelength position versus cross arm length, (b) absorption magnitude versus cross arm length and (c) Q value versus cross arm length for the 4 different SiO_2 thicknesses.

Figure 4 compares the experimental and simulation data for the (a) peak absorption wavelength versus cross arm length, (b) peak absorption magnitude versus cross arm length and (c) Q value versus cross arm length. The simulation and experimental data shows excellent agreement in terms of the general trends. However the simulated peak absorption wavelength position is underestimated compared to the experimental one by an average of 0.48 μm. This is most likely due to the refractive index of the PECVD SiO_2 differing from the simulated values used in Lumerical FDTD software. It is well established that as the refractive index of the dielectric layer increases the peak absorption wavelength position redshifts [18]. We also see that there is a linear relationship of the cross arm length versus the peak absorption wavelength position. The experimental 100 nm thick SiO_2 data has a relationship of $\lambda_p = 0.0029l + 0.7189$ where λ_p is the peak absorption wavelength position. Using this equation we can determine the cross arm length required to attain close to unity absorption at any wavelength between 3.08 μm and 5.6 μm.

Comparing the peak wavelength absorption magnitude for the simulation and experimental data, see Fig. 4(b), we see that a thicker SiO_2 layer is required to experimentally realise unity absorption. Again, this discrepancy can be attributed to the loss component, *k*, of our PECVD SiO_2 differing from the simulated value. In any hyperspectral application the

filter or absorber should have high spectral selectivity. In effect this translates to a high Q factor, where Q = λ_p/full width-half maximum. In Fig. 4(c) we plot the Q value for the simulation and experimental data. For the simulation data the maximum Q value attained is 12 while the average is 10.1 for all 40 metamaterial absorbers. Q values of the fabricated devices are slightly smaller, averaging 7.3. For the absorbers with the largest absorption magnitude (100 nm thick SiO_2), the maximum Q attained is 8.5 while the average is 7.7. Our experimental Q values are typical of single band cross shaped ERR MIM metamaterial absorbers

4. Incident Angle Dependence and Observation of a Fano Resonance

In this section we examine the spectral response characteristics of the CMOS compatible metamaterial absorbers for obliquely incident radiation ranging from 0° to 60° for both transverse electric (TE) and transverse magnetic (TM) polarisations. This is an important and often overlooked consideration when proposing metamaterial absorbers be integrated with detectors to form imaging array systems. In an imaging system, depending on the numerical aperture of the lens and the size of the focal plane array, the MWIR radiation incident on the sensor can vary from 0° to +/−30° [34]. Ideally, there should be no deviation of either the absorption magnitude or peak wavelength position as the angle of incidence or polarisation varies.

Figure 5 shows the simulated incident angle dependence for both TE and TM polarised light for metamaterial absorbers with a SiO_2 thickness of 75 nm and varying cross arm lengths from 800 to 1700 nm in steps of 100 nm. The simulation set-up is shown in the inset of Fig. 1(a) where the incident angle, φ, is varied in the xz plane. For TM the e-field is polarised in the x axis direction while for TE the e-field is polarised in the y axis direction. From the simulation results we see that for the majority of the metamaterial structures the absorption properties remain constant both in terms of absorption magnitude and wavelength peak position for all angles up to 60° and for both polarisations. The only situations where this is not so are for cross arm lengths of 800 nm [Figs. 5(a) and 5(k)] 900 nm [Figs. 5(b) and 5(l)] and 1000 nm (Figs. 5(c) and 5(m)] where the absorption characteristics are constant up to incident angles of 25°, 35° and 45° respectively. For the case of TE polarised light, beyond these angles the absorption magnitude slowly starts to decrease with the wavelength peak position remaining relatively constant. This behaviour is attributed to the parallel magnetic field component approaching zero as the incident angle increases and being unable to effectively induce antiparallel currents in the ERR layer and the ground plane resulting in a drop in the magnetic flux [35]. For the case of TM polarised light the drop-off in absorption magnitude is a result of a second mode interfering with the metamaterial absorber mode. This mode is attributed to surface plasmon polaritons (SPPs) occurring between the metallic ground plane and the SiO_2 layer. On a continuous metal film SPPs can only be generated for TM polarised light, they do not occur for TE polarised light [36]. To further support our physical explanations for the reduction in absorption magnitude with incident angle for both TE and TM polarisations we show in Fig. 6 the simulated spectral response characteristics of metamaterial absorbers for the 4 experimentally studied SiO_2 spacer thicknesses and for cross arm lengths of 800 and 1700 nm. It is clear for all spacer thicknesses that when l = 800 nm and the incident light is TE polarised there is a critical angle after which the magnetic resonance and therefore absorption magnitude is diminished while when the incident light is TM polarised there is a shorter wavelength SPP mode that red shifts with increasing angle until it destructively interferes with the metamaterial induced absorption mode. We also investigated via Lumerical FDTD simulations the absorption characteristics with varying azimuthal angle. The azimuthal angle was fixed at 0°, 30° and 60° and the polar angle varied for both TE and TM polarisations. Since the cross shaped ERR is symmetric there should be

no change in the absorption properties with varying azimuthal angle which the FDTD simulations confirmed.
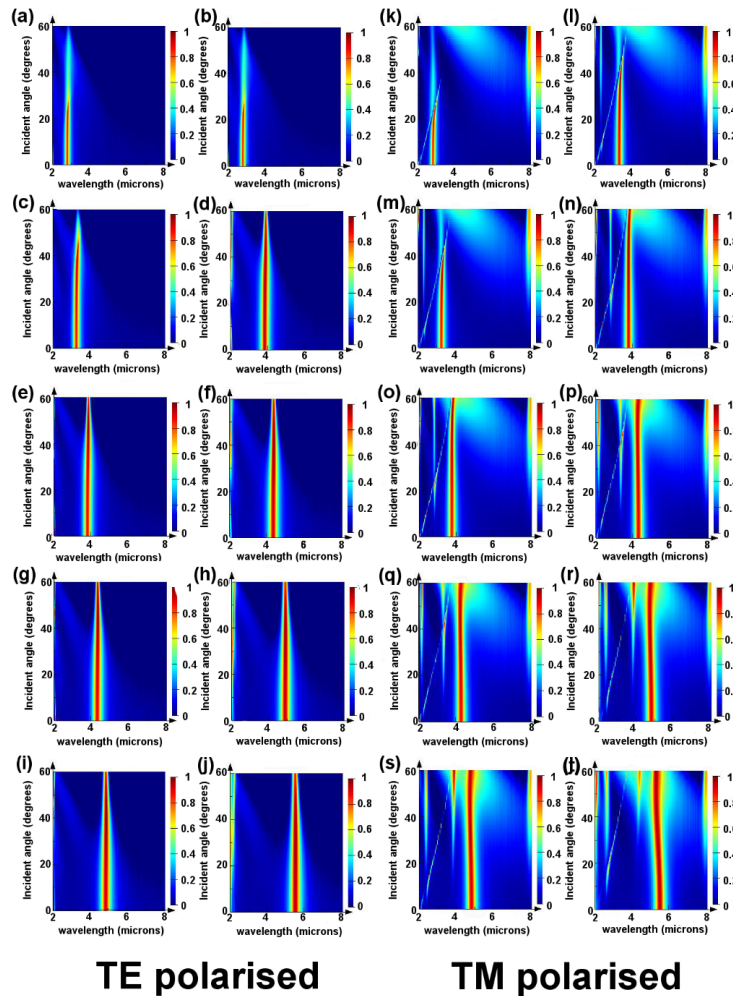

TE polarised   **TM polarised**

Fig. 5. Spectral absorption intensity for incident angles up to 60° for the CMOS compatible MWIR metamaterial absorbers with a 75 nm thick SiO_2 spacer for both TE and TM polarisations and varying cross arm lengths. TE data is shown for cross arm lengths of (a) 800 nm, (b) 900 nm, (c) 1000 nm, (d) 1100 nm, (e) 1200 nm, (f) 1300 nm, (g) 1400 nm, (h) 1500 nm, (i) 1600 nm and (j) 1700 nm. TM data is shown for cross arm lengths of (k) 800 nm, (l) 900 nm, (m) 1000 nm, (n) 1100 nm, (o) 1200 nm, (p) 1300 nm, (q) 1400 nm, (r) 1500 nm, (s) 1600 nm and (t) 1700 nm.

The interference between the metamaterial absorber mode and the SPP mode could be of benefit since at specific angles there is a Fano type behaviour where multiple asymmetric absorption peaks are observed [37]. For example, Fig. 7(a) shows the simulated absorption spectral characteristics for l = 800 nm, t = 75 nm and TM polarisation for different incident angles. Some of the absorption peaks have ultra-narrow linewidths resulting in Q factors as high as 51.5 (30° incident angle) and would be extremely useful in sensing applications that require high spectral selectivity such as hazardous gas identification. To better understand the characteristics of this SPP mode we replaced the SiO_2 dielectric spacer with a Si_3N_4 spacer and simulated different metamaterial absorber structures. For the n and k of the Si_3N_4 we used values published by Kischkat [38]. Figure 7(b) shows the spectral absorption characteristics

for different polar incident angles for a 75 nm thick Si_3N_4 dielectric spacer and cross arm length of 800 nm for TM polarisation. Analogous to the absorbers with a SiO_2 spacer there is a strong angle independent metamaterial absorber mode and an angle dependent SPP mode occurring at shorter wavelengths that again red shifts with increasing incident angle. Figure 7(c) shows the simulated spectral absorption characteristics at normal incidence for metamaterial absorbers with a 75 nm Si_3N_4 dielectric spacer and varying cross-arm lengths. The higher refractive index of Si_3N_4 compared to SiO_2 means that the absorption peak occurs at longer wavelengths, e.g. when l = 800 nm the absorption peak is at 4.23 μm for Si_3N_4 compared to a simulated absorption peak value of 2.72 μm and experimental value of 3.01 μm for SiO_2. The larger refractive index of Si_3N_4 also means that in the 2-8 μm range higher order modes can be accessed. In Fig. 7(d) we plot the dispersion curves for the SPP absorption peak for metamaterial absorbers with a SiO_2 thickness of 75 nm and cross arm lengths from 800 to 1700 nm and for a metamaterial absorber with a 75 nm Si_3N_4 dielectric spacer and a cross arm length of 1700 nm. Note that the shown data is only for angles when the SPP absorption peak was far away from the metamaterial absorption peak. It is clear from the graph that the SPP mode is essentially independent of the metamaterial cross arm length and dielectric spacer type. The dominating factor determining the position of the SPP absorption peak is the unit cell period. This is confirmed by Figs. 7(e) and 7(f) where we show the spectral absorption intensity for varying incident angles for a metamaterial absorber with a smaller period than those studied thus far (1000 nm), SiO_2 dielectric spacer thickness of 75 nm and cross arm length of 800 nm for both TM and TE polarisations. The metamaterial absorber mode intensity is essentially unchanged for incident angles up to 60° for both TM and TE polarisation. These results show that selecting the appropriate unit cell size is essential in designing hyperspectral, omni-directional, polarisation insensitive metamaterial absorbers.
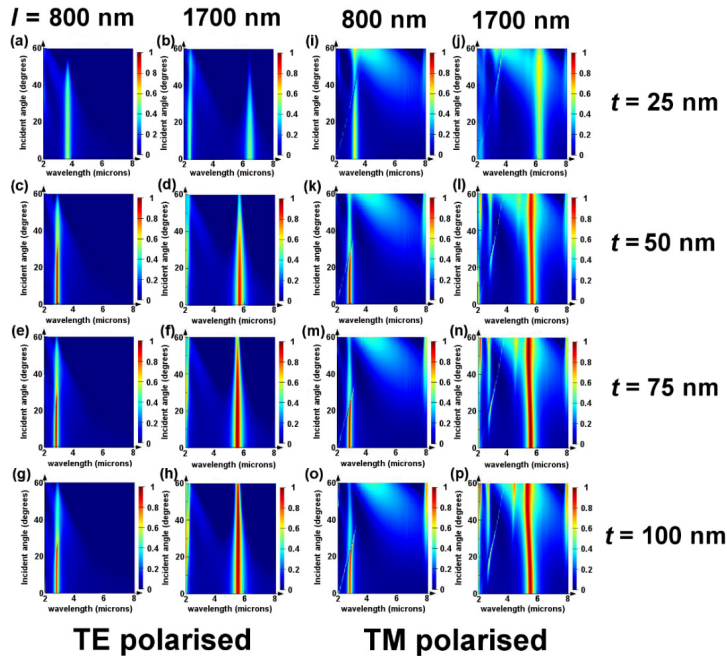

Fig. 6. Spectral absorption intensity for incident angles up to 60° for the CMOS compatible MWIR metamaterial absorbers with different SiO_2 spacer thicknesses for both TE and TM polarisations for cross arm lengths of 800 nm and 1700 nm. (a), (c), (d), (g), (i), (k), (m) and (o) are for cross arm lengths of 800 nm. (b), (d), (e), (h), (j), (l), (n) and (p) are for cross arm lengths of 1700 nm.
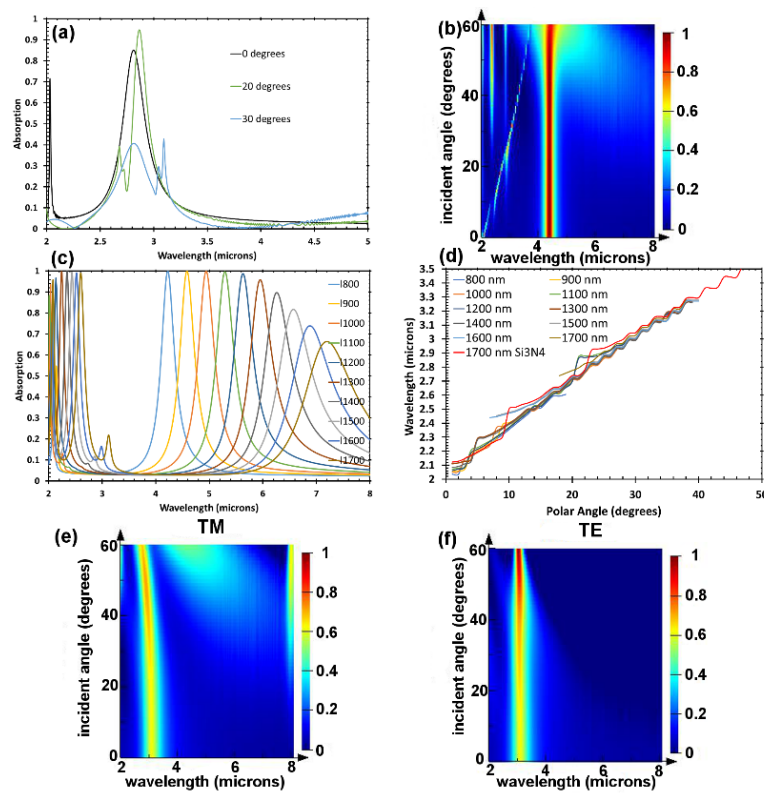
Fig. 7. Observation of a Fano resonance. (a) Interference between the metamaterial absorber mode and the surface plasmon polariton mode (SPP) results in Fano resonant behaviour at 20° and 30° oblique incident angles for a metamaterial absorber with a SiO_2 spacer thickness of 75 nm and cross arm length of 800 nm. (b) Spectral absorption characteristics for differing incident angles for a metamaterial absorber with l = 800 nm where the 75 nm dielectric spacer is Si_3N_4 instead of SiO_2. Spectral absorption characteristics at normal incidence for metamaterial absorbers with a 75 nm Si_3N_4 dielectric spacer and varying cross-arm lengths. (d) Dispersion relationship of the SPP absorption peak for metamaterial absorbers with a SiO_2 thickness of 75 nm and varying cross arm lengths and for a metamaterial absorber with a 75 nm Si_3N_4 dielectric spacer and a cross arm length of 1700 nm. Spectral absorption intensity for incident angles up to 60° for a metamaterial absorber with period = 1000 nm, SiO_2 dielectric spacer thickness of 75 nm and cross arm length of 800 nm for both (e) TM and (f) TE polarisations.

Finally, in Fig. 8 we compare our cross-shaped ERR geometry with circle and square ERRs of identical diameter and side length respectively for a SiO_2 dielectric spacer thickness of 75 nm. For all ERR shapes the absorption magnitude exceeds 98% (not shown). In terms of the wavelength peak position, cross and circle shaped ERRs are almost identical for arm/side lengths from 800 to 1700 nm. Square shaped ERRs however consistently have resonance peaks at longer wavelengths compared to cross and circle shaped ERRs. Figure 8(b) shows how the Q value compares between cross, circular and square shaped ERRs. It is clear to see that cross shaped ERRs have larger Q values and are therefore more resonant than square or circle shaped ERRs. Clearly, for hyperspectral imaging applications it is advantageous to have a large Q value therefore it is best to use cross shaped ERRs rather than circular or square shaped ERRs.
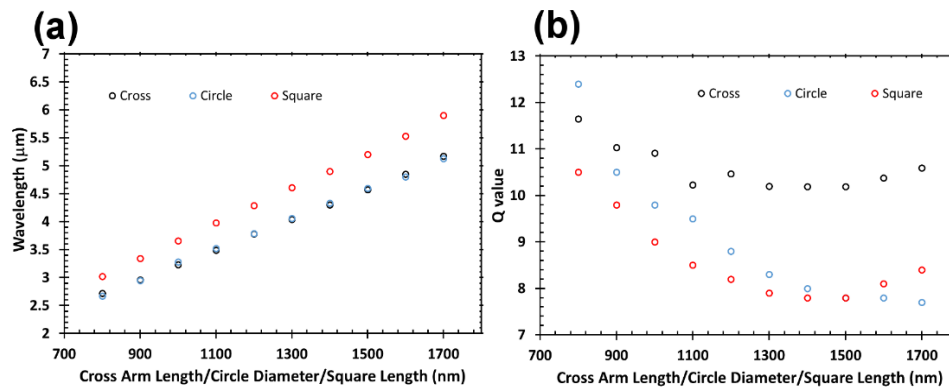
Fig. 8. Analysis and comparison of simulation data for the CMOS MWIR metamaterial absorbers of cross, circular and square shaped ERRs with a SiO$_2$ dielectric spacer thickness of 75 nm. (a) wavelength peak position and (b) Q value.

5. Conclusion

In summary we have experimentally detailed and described a CMOS compatible metal-insulator-metal metamaterial absorber geometry where for a single SiO$_2$ spacer thickness of 100 nm a minimum of 93% absorption is attained for 10 separate bands centred at 3.08, 3.30, 3.53, 3.78, 4.14, 4.40, 4.72, 4.94, 5.33, 5.60 μm throughout the MWIR spectrum. We have also revealed that the absorption characteristics of the hyperspectral metamaterial structures are invariant up to incident angles up to 25° making them suitable for implementation in an imaging system. Our hyperspectral MWIR metamaterial absorbers can be integrated with bolometric or pyroelectric detectors and formed into highly sensitive low-cost focal plane arrays. Such a hyperspectral MWIR imager has numerous applications in areas such as gas detection, identification of biological materials, chemical sensing and imaging and pollution monitoring. Our hyperspectral metamaterial device could also be used for applications that require selective thermal emission (e.g. energy harvesting) since according to Kirchoff's laws the emissivity of a material is equal to its absorptivity [14]. Furthermore, by perforating the ground plane of the MWIR metamaterial absorbers with arrays of sub-wavelength nanoholes that selectively filter visible light we can hybridize plasmonic metasurface and metamaterial absorber technologies to form a synthetic multi-spectral material that can simultaneously selectively absorb MWIR and filter visible [39–41]. Coupling with appropriate detectors, namely pyrometers or bolometers for the MWIR and CMOS Si photodiodes for the visible, we can render a CMOS based, real-time and low-cost co-axial hyperspectral MWIR and visible imager.